Production-scale fibronectin nanofibers promote wound closure and tissue repair in a dermal mouse model

Christophe O. Chantre [a, b], Patrick H. Campbell [a], Holly M. Golecki [a], Adrian T. Buganza [a, c], Andrew K. Capulli [a], Leila F. Deravi [a, e], Stephanie Dauth [a], Sean P. Sheehy [a], Jeffrey A. Paten [d], Karl Gledhill [f], Yanne S. Doucet [f], Hasan E. Abaci [f], Seungkuk Ahn [a], Benjamin D. Pope [a, g], Jeffrey W. Ruberti [d], Simon P. Hoerstrup [b], Angela M. Christiano [f], Kevin Kit Parker [a, *]

[a] Disease Biophysics Group, Wyss Institute for Biologically Inspired Engineering, John A. Paulson School of Engineering and Applied Sciences, Harvard University, Cambridge, MA, USA
[b] Institute for Regenerative Medicine, University of Zurich, ZH, Switzerland
[c] Department of Mechanical Engineering, Purdue University, West Lafayette, IL, USA
[d] Department of Bioengineering, Northeastern University, Boston, MA, UK
[e] Department of Chemistry and Chemical Biology, Northeastern University, Boston, MA, USA
[f] Department of Dermatology, Columbia University, New York, NY, USA
[g] Beth Israel Deaconess Medical Center, Harvard Medical School, Boston, MA, USA

ARTICLE INFO

ABSTRACT

Wounds in the fetus can heal without scarring. Consequently, biomaterials that attempt to recapitulate the biophysical and biochemical properties of fetal skin have emerged as promising pro-regenerative strategies. The extracellular matrix (ECM) protein fibronectin (Fn) in particular is believed to play a crucial role in directing this regenerative phenotype. Accordingly, Fn has been implicated in numerous wound healing studies, yet remains untested in its fibrillar conformation as found in fetal skin. Here, we show that high extensional (~1.2 $\times$ 10^5 s^{-1}) and shear (~3 $\times$ 10^5 s^{-1}) strain rates in rotary jet spinning (RJS) can drive high throughput Fn fibrillogenesis (~10 mL/min), thus producing nanofiber scaffolds that are used to effectively enhance wound healing. When tested on a full-thickness wound mouse model, Fn nanofiber dressings not only accelerated wound closure, but also significantly improved tissue restoration, recovering dermal and epidermal structures as well as skin appendages and adipose tissue. Together, these results suggest that bioprotein nanofiber fabrication via RJS could set a new paradigm for enhancing wound healing and may thus find use in a variety of regenerative medicine applications.

© 2018 Elsevier Ltd. All rights reserved.

1. Introduction

Developing dressings that restore cutaneous wounds to their original, healthy state remains a clinical challenge that impacts millions of people every year [1]. In the absence of external intervention, acute wounds and severe burns often result in collagen-dense scar formation as well as incomplete regeneration of hair follicles, sebaceous glands and cutaneous fat [2,3]. Adverse consequences can also include decreased tissue strength, elasticity, and impaired joint mobility [4,5], while changes in cosmetic appearance can lead to psychological sequelae. Several therapeutic strategies have emerged over the last decades to improve the suboptimal outcome of normal wound healing. For instance, biomaterials derived from natural hydrogels have been developed to stimulate the wound healing process by supporting cellular ingrowth and stimulating pro-regenerative behavior through precise biomechanical and biochemical cues [6–8]. To improve wound stability and tissue integration, mechanical and structural features like degradation rate, porosity and water absorbance have also been investigated [9–12]. Although development of these functional materials has led to reduction in infection rates, tissue morbidity and scar formation, none of these strategies have been able to restore skin tissue to its native *scarless* configuration [13,14].

During embryogenesis, scarless wound healing is a characteristic phenomenon observed through the end of the second trimester [15]. Although the mechanisms that regulate this regenerative phenotype are not fully understood, several spatiotemporal differences of the extracellular microenvironment have been observed in fetal and postnatal wounds [16,17] providing creative insight for wound dressing design [18]. The ECM protein fibronectin (Fn) in particular is involved in gestational wound healing in contrast to adults and has inspired the development of novel therapeutics [19]. For example, when Fn-binding domains were adsorbed or tethered to hyaluronan-based scaffolds, they increased cell binding [20] and supported wound healing *in vivo* [21]. Moreover, recombinant fragments of Fn containing one or more functional domains, created favorable microenvironments that accelerated wound healing in diabetic mice [22,23].

Fn exists in two distinct conformations *in vivo*: a globular, soluble state and an extended fibrillar state. While globular Fn has been shown to stimulate angiogenesis, reduce the inflammatory response, and increase the rate of wound closure [24,25], there is limited information on how fibrillar Fn — the highly upregulated form in fetal wound microenvironments — can be leveraged as a material for wound healing. Fibrillar Fn is critical during tissue repair [26], and its structural stability in a proteolytic environment, characteristic of cutaneous wounds [27] suggest advantages for promoting robust cellular ingrowth and directing pro-regenerative cell function in the wound. However, manufacturing fibrillar Fn remains an engineering challenge, as the available chemical [28,29], mechanical [30,31] or extrusion [32] methods of producing fibers are limited to small (~mm) scales. In order to recapitulate the Fn-rich fetal microenvironment at a scale suitable for clinical applications, new methods are required for the production and assembly of fibrillar Fn networks. We reasoned nanofiber manufacturing techniques such as rotary jet spinning (RJS) could be employed for the bulk production of Fn scaffolds. The RJS is indeed distinct among other nanofiber manufacturing techniques, as it utilizes centrifugal forces, instead of electric field gradients or high solution temperatures [33,34], to eject a biopolymer jet from a micron-sized orifice to produce nanoscale fibers [35,36]. Its process parameters such as nozzle diameter and spinning velocity can be tuned for different material types, improving morphological quality of fibers [37,38]. We thus hypothesized that the centrifugal forces of the RJS could be used to generate fluid strain rates necessary to unfold the soluble, globular Fn molecule, facilitating fibrillogenesis and protein network formation. The bulk production capability of the RJS could enable assembly of large sheets of fibrillar Fn, required for the development of regenerative materials.

In this study, we show that RJS can fabricate centimeter-wide, thick (>100 μm) wound dressings out of pure fibrillar Fn. Analytical and computational simulations developed in parallel validate how the extensional and shear flow regimes in the rotating reservoir are sufficient to extend the globular conformation, thus enabling flow-induced fibrillogenesis. Using fluorescence resonance energy transfer (FRET), we confirm Fn molecular unfolding induced by the hydrodynamic forces applied to the protein. Fn scaffolds are then investigated as a bioactive material strategy for accelerating wound closure and promoting skin tissue restoration in a full-thickness wound mouse model. To evaluate the regenerative potency of our Fn dressings, treated-skin tissues are systematically compared to healthy native skin by assessing restoration of basic structural components like epidermal thickness and hair follicles density. Non-treated wounds are added as a comparison control group. A skin tissue architecture quality (STAQ) index, developed to respond to the paucity in regenerative performance standards in pre-clinical experiments, is furthermore utilized as a quantitative metric for comparing our different treatments. It

highlights the capacity of Fn nanofiber scaffolds to recover a skin architecture close to healthy skin, and stresses the skin components that still require improvement. Taken together, these data show that synthetic fibrillogenesis is effective for manufacturing fibrillar Fn nanofiber wound dressings and subsequently demonstrates promise as a pro-regenerative material strategy, exhibited by accelerated wound closure and enhanced tissue restoration.

2. Materials and Methods

2.1. Protein nanofiber fabrication

The RJS set-up consists of a custom machined aluminum reservoir with an inner diameter of 20 mm and volume of 3.5 mL perforated with two cylindrical orifices (D = 400 μm, L = 0.75 cm) (Fig. 1a and b). The perforated reservoir was attached to the shaft of a brushless motor (Maxon motors, Fall River, MA) and rotation speed, ranging from 10 k rpm to 35 k rpm, was controlled by circuit board. *Fn nanofiber fabrication:* Fn was obtained (Human, BD Biosciences) as a 5 mg lyophilized powder in its unreduced form with a molecular weight of 440 kDa. To facilitate dissolution of Fn and appropriate solvent evaporation to form nanofibers, a 2:1 mixture of 1,1,1,3,3,3-Hexafluoro-2-propanol (HFIP) (Sigma Aldrich, St. Louis, MO) and millipore H_2O was used as a solvent. 2% weight/volume (w/v) Fn was first dissolved in millipore H_2O for 24 h at 4 °C and prior to spinning HFIP was added. After the motor reached target speed, Fn solution was loaded by pipette at a rate of ~10 mL/min into the perforated reservoir. The resulting fibers were collected on a stationary round collector of radius = 13.5 cm. The collector was lined with 25 mm glass coverslips to collect fibers. Alternatively, samples were collected on a rotating mandrel, forming sheets of Fn nanofibers (Movie S1 and Fig. S1).

Supplementary video related to this article can be found at https://doi.org/10.1016/j.biomaterials.2018.03.006.

2.2. Nanofiber diameter measurements

Fibers were removed from the collector and sputter coated with 5 nm Pt/Pd (Denton Vacuum, Moorestown, NJ) to minimize charging during imaging. The samples were imaged using a Zeiss SUPRA 55 field-emission scanning electron microscope (Carl Zeiss, Dresden, Germany). Images were analyzed using image analysis software (ImageJ, NIH). A total of 100—200 fibers were analyzed (3—6 random fields of view per sample) to calculate the fiber diameter. The fiber diameter distribution was reported as mean fiber diameter ± standard error of the mean (SEM).

2.3. Protein structural integrity

To ensure that Fn proteins remained intact after dissolution in HFIP solvent (for a period of 5 h maximum) and subsequent unfolding into nanofibers, Raman spectroscopy analysis was performed, suggesting Amide stretching regions (Fig. S2). Briefly, spectral scans were collected using a WITec Confocal Raman microscope/SNOM/AFM (WITec, Alpha300) with a 532 nm laser. Three spectral scans (Integration time = 25 s) were collected for n = 10 fibers per sample.

2.4. Fn immunostaining

Fn fibers were stained by incubating fiber coated coverslips in a solution of PBS containing a 1:200 dilution of anti-human Fn polyclonal antibody (Sigma) for 1 h at room temperature. Samples were rinsed in PBS (3 × 15 min). Samples were then incubated in a 1:200 dilution of Alexa Fluor 546 goat anti-rabbit IgG (H+L)

secondary antibody (Invitrogen, Eugene, OR) for 1 h. After staining, samples were rinsed and mounted on glass slides for imaging. Images were then acquired on the LSM 5 LIVE Confocal Microscopy (Carl Zeiss) using a 40X/1.3 Oil Differential Interference Contrast (DIC) objective lens. Fn labeled with Alexa Fluor 488 was imaged with a $\lambda = 488$ nm wavelength emission laser. Nanofibers immunofluorescently-labeled were imaged using a $\lambda = 546$ nm wavelength emission laser.

2.5. Fn FRET measurements

Fn molecules were FRET-labeled according to previously published protocols [39–42]. Briefly, Fn was denatured in 4 M guanidinium hydrochloride [GdnHCl] for 15 min, then incubated with tetramethylrhodamine-5-maleimide (TMR) (Molecular Probes, Invitrogen) at room temperature for 2 h to covalently bind TMR to cryptic cysteines by maleimide coupling. Fn was then refolded and separated from unreacted TMR fluorophore by size exclusion chromatography (Quick Spin G-25 Sephadex Protein Columns, Roche). TMR labeled Fn was then incubated with Alexa Fluor 488 carboxylic acid, 2,3,5,6-tetrafluorophenyl ester (Molecular Probes, Invitrogen) for 1 h at room temperature. The dual-labeled Fn was separated from unreacted fluorophore using size exclusion chromatography. Dual-labeled Fn was then lyophilized and used immediately. Using confocal microscopy, samples were excited at $\lambda = 488$ nm and emission spectra was collected at $\lambda = 520$ nm and 576 nm. Fluorescent images were analyzed using ImageJ image analysis software.

2.6. Fn nanofiber tensile testing

Mechanical testing of Fn nanofibers was performed according to previously published methods [42] using glass micropipette beam bending. Solid borosilicate glass rods (#BR-100-10, diameter: 1.0 mm, length: 10 cm, Sutter Instrument Co., Novato, CA) were pulled into tapered pipettes using a Flaming/Brown Micropipette Puller (Sutter Instrument Co.) by the following parameter settings: Heat = 730, Pull = 50, Velocity = 100, Time = 250. Calibrated pipettes were then used to measure force generated during single fiber tensile tests [42]. Fn nanofibers were attached at one end to a calibrated pipette and at the other to a force applicator pipette via nonspecific adhesive forces. Samples were then pulled uniaxially at a constant strain rate of 1 μm s-1 (Fig. S3).

2.7. In vivo wound healing studies

All animal experiments were performed following a procedure approved by the Harvard University Institutional Animal Care and Use Committee (IACUC). C57BL/6 male mice (52 days old) (Charles River Laboratories, Wilmington, MA) were anesthetized and maintained on surgical plane of anesthesia with isoflurane. Once a toe pinch test confirmed anesthesia, the dorsal side of mice were prepared by shaving with an electric razor and then a manual razor. The surgical area was cleaned three times with betadine and alcohol to sterilize the area. Two full thickness wounds were made on the back, lateral to the spin on both sides and nanofiber dressings were applied to the wound. Following previous wound healing protocols that studied de novo regeneration of hair follicles, no splinting model was used in these experiments [43,44]. To keep the area clean, free of debris and stabilized, Tegaderm™ patches were applied above all treatment conditions and left until they naturally detached within 4–6 days. Mice were monitored daily. After 20 days, mice were sacrificed via IACUC approved methods and tissue harvested for further testing. To confirm mouse health for the duration of the study, the mice were weighed at the beginning and

ending of the study and were all shown to gain on an average 2.7 g over a 3-week study. There was no significant weight or health difference in any test or control group.

2.8. Wound closure measurements

Wound area was measured from digital photographs of wounds taken every two days throughout the study. Area was measured by tracing leading edge of the epithelial layer using ImageJ image analysis software.

2.9. Histological and immunofluorescent staining

Tissues were harvested from healthy and injured mice and fixed with 4% paraformaldehyde for 5 min. To stain and image tissues, we then used a cryostat operation to prepare thin slices from the harvested tissues. We first embedded whole tissues in either a 50% Paraffin and 50% Tissue-Tek O.C.T Compound embedding medium solution (Electron Microscopy Sciences, Hatfield, PA) or in a 100% Tissue-Tek O.C.T Compound embedding medium solution for 24 h, after which samples were flash frozen in liquid nitrogen and stored at $-20\,^{\circ}$C. Thin slices were then prepared with a Leica CM 1950 cryostat and collected with Super Frost Plus slides, after which they were replaced in a freezer at $-20\,^{\circ}$C before staining. Next, staining and imaging were performed according to standard protocols and are detailed in SI Materials and Methods.

2.10. Epidermal thickness quantification

Recovery of healthy epidermal structure in our treated tissues was assessed by measuring epidermal thickness from Masson's Trichrome staining tissue sections. Thickness was measured manually using ImageJ image analysis software. Fig. S4 illustrates measurements of different treated tissue samples, calculated between the black dashed lines. Lower dashed black lines were drawn at the interface of the dermis and the stratum basal, and the upper dashed black line was positioned above the stratum granulosum, disregarding the stratum corneum as it flaked off during staining.

2.11. Hair follicle and sebaceous gland quantification

Density of skin appendages in our treated tissues was quantified by counting hair follicles and sebaceous glands in Masson's trichrome stained tissue sections (Fig. S4). As wound closure in mice is strongly promoted by contraction compared to humans [45], consistency in measurements was maintained by establishing wound edges. The wound edges were defined by determining the position where the underlying panniculus carnosus muscle tissue was sectioned as illustrated in Fig. S5. Hair follicle and sebaceous gland amounts were quantified per area and compared to healthy native tissues (Fig. S4).

2.12. ECM fiber alignment quantification

Organization of ECM fiber alignment was quantified using a dimensionless value (coherence), from 0 for perfectly isotropic to 1 for perfectly anisotropic, as described previously [46]. Briefly, Masson's trichrome images were cropped to the region of interest and analyzed using the OrientationJ plugin available on ImageJ software. The coherence is directly computed and used to assess ECM fiber orientation.

2.13. Adipocyte area coverage

The amount of adipose tissue was assessed by ratio of the area

covered with adipocytes to the total area of interest. As detailed previously [47], we used a semi-automated method to quantitatively analyse adipocyte coverage using ImageJ analysis software. Masson's trichrome tissue sections were thresholded and converted to binary images, thus enabling size measurement of individual adipocytes.

2.14. Development of a skin tissue architecture quality (STAQ) index

To quantitatively assess the efficacy of nanofiber wound dressings to promote tissue restoration, we developed a Skin Tissue Architecture Quality (STAQ) index. This rubric utilizes a modified form of the Hellinger distance metric used previously to assess the therapeutic outcome of cardiopoietic stem cell repair of myocardial infarction [48] to calculate the overlap in values from 5 experimentally-measured parameters (e.g. epidermal thickness, ECM fibers alignment, hair follicle density, sebaceous gland density, and percent adipocyte coverage) between healthy/unwounded skin and wounded skin that has been treated with a wound dressing. The STAQ index (Eq. (1)) uses the mean (μ) and standard deviation (σ) values of the experimental measurements from healthy and wounded skin to calculate the degree of separation between the probability distributions for each experimental parameter.

$$STAQ = 100 \times \left(1 - \sqrt{\frac{2\sigma_{healthy}\sigma_{wounded}}{\sigma_{healthy}^2 + \sigma_{wounded}^2}} \; e^{-\frac{1}{4}\frac{\left(\mu_{healthy} - \mu_{wounded}\right)^2}{\sigma_{healthy}^2 + \sigma_{wounded}^2}} \right)$$
(1)

The STAQ score output by this equation falls within the interval [0, 100], where a score of zero indicates that the population distributions are completely different (i.e. no match between healthy and wounded skin), and a value of 100 indicates that they are completely identical (i.e. perfect match between healthy and wounded skin). Combined scores for each wound dressing were calculated as the mean absolute deviation (MAD) between the healthy and wounded STAQ scores (Eq. (1)) for the set of 5 experimental parameters measured, according to the following equation:

$$MAD = \frac{1}{n} \sum_{i=1}^{n} \left| STAQ_{wounded,i} - STAQ_{healthy,i} \right|$$
(2)

where n represents the number of experimental parameters, $STAQ_{wounded}$ represents the STAQ scores for the index parameters from mice that were wounded and treated with wound dressings and $STAQ_{healthy}$ represents the STAQ scores for the index parameters from the unwounded skin of healthy mice.

2.15. Statistical analysis

Statistical analyses were conducted using SigmaPlot (v12.0, Systat Software, Inc., CA). One-way ANOVA on ranks with post hoc multiple comparisons Dunn's test, or Holm-Sidak's test, and Student's t-test were used where appropriate, for wound closure and histological data analyses. Quantitative data are presented as mean ± SEM and significance was considered for $p < 0.05$.

3. Results and discussion

3.1. Synthetic fibrillogenesis of Fn nanofibers

We first utilized analytical and computational models to estimate whether the strain and shear rates generated in the RJS could induce Fn unfolding and fibrillogenesis (Fig. 1a and Fig. S6 and SI Notes S1-S4). To establish these models, we separated the system into its two distinct flow regimes: the transitory entry flow, where the fluid travels from the reservoir to the channel, and the channel flow, where the fluid travels through the channel and is ejected out of the system (Fig. 1a–c and Fig. S6). Once the fluid exits the reservoir channel, it will be exposed to sudden lateral forces while the solvent gradually evaporates. Fiber formation and extension will ensue, enabling assembly of nanofiber sheets on a collector (timescale ~ 0.01s) [35–38].

We focus on a first step on the entry flow where the Fn solution will experience acceleration as it is constricted into the channel (Fig. 1c, top schematic). This acceleration, characterized by high extensional strain rates, was recently described to enable and drive protein aggregation in a similar system [49]. Thus, to evaluate the propensity of Fn to undergo fibrillogenesis in this flow regime, we calculated the velocity profile and extensional strain rates using computational fluid dynamics (CFD) simulations (Fig. 1c and Fig. S7). The strain rates for a rotation speed of ~28′000 rpm were estimated at 0.76×10^5 s^{-1} along the center line and at 1.28×10^5 s^{-1} proximal to the entry flow edges. Next, we calculated the Deborah (De) number, used to explain the conformational changes of proteins under elongation flow (SI Notes S2):

$$De = \tau_r \, \dot{\varepsilon}$$
(3)

Equation (3) expresses the dimensionless number De that quantifies the deformation rate $\dot{\varepsilon}$ and the protein's relaxation time relation, with τ_r the longest relaxation time − estimated at 222 μs for Fn (SI Notes S2). From this, we calculated a De number of 28.9 (Fig. S8). In contrast, previous experiments showed that stretching of DNA was achieved with a De as low as 4.1 [50,51]. This suggests that the elongation strain rates in RJS should be sufficient to initiate unfolding of Fn. Alternatively, calculating the total work applied to an Fn molecule as it moves from the reservoir to the channel also demonstrated comparable values to previously described methods of Fn nanotextile fabrication [42]. Another consideration is the balancing of the drag forces and the tension in the molecule as it is extended. Modeling Fn as a worm-like chain reveals an equilibrium stretch of 0.98 for the strain rate calculated above (SI Notes S2 and S4).

Although elongation flow described above is likely the strongest contributor to Fn unfolding [49], shear has likewise been demonstrated to impact protein conformation [52]. To determine the shear rate produced in the RJS channel, we assumed a Poiseuille flow and calculated the pressure gradient along the channel as a function of the centrifugal force exerted by the rotating reservoir (Fig. 1c and SI Notes S3). Shear rates achievable within the RJS system therefore range from 0 to ~3×10^5 s^{-1}. CFD simulations in the channel paralleled our calculations (Fig. 1c). Next, as varying shear rates from the centerline to the channel wall can have a significant effect on molecular extension dynamics [52], we calculated the Weissenberg (Wi) number that has been used to explain conformational changes in such conditions (SI Notes S3):

$$Wi = \dot{\gamma} \, \tau_r$$
(4)

Equation (4) shows the nondimensional Wi number dependent on the shear rate $\dot{\gamma}$ and the relaxation timescale introduced earlier, and is readily calculated at 79.0 for the maximum rotation speed at the channel wall (Fig. S8). From simulations previously described [53], normalized molecular extension reaches an asymptotic limit close to 0.5 for a Wi number approaching 80, thus suggesting that shear-induced conformational changes of Fn should be achievable within our system (SI Notes S3 and S4).
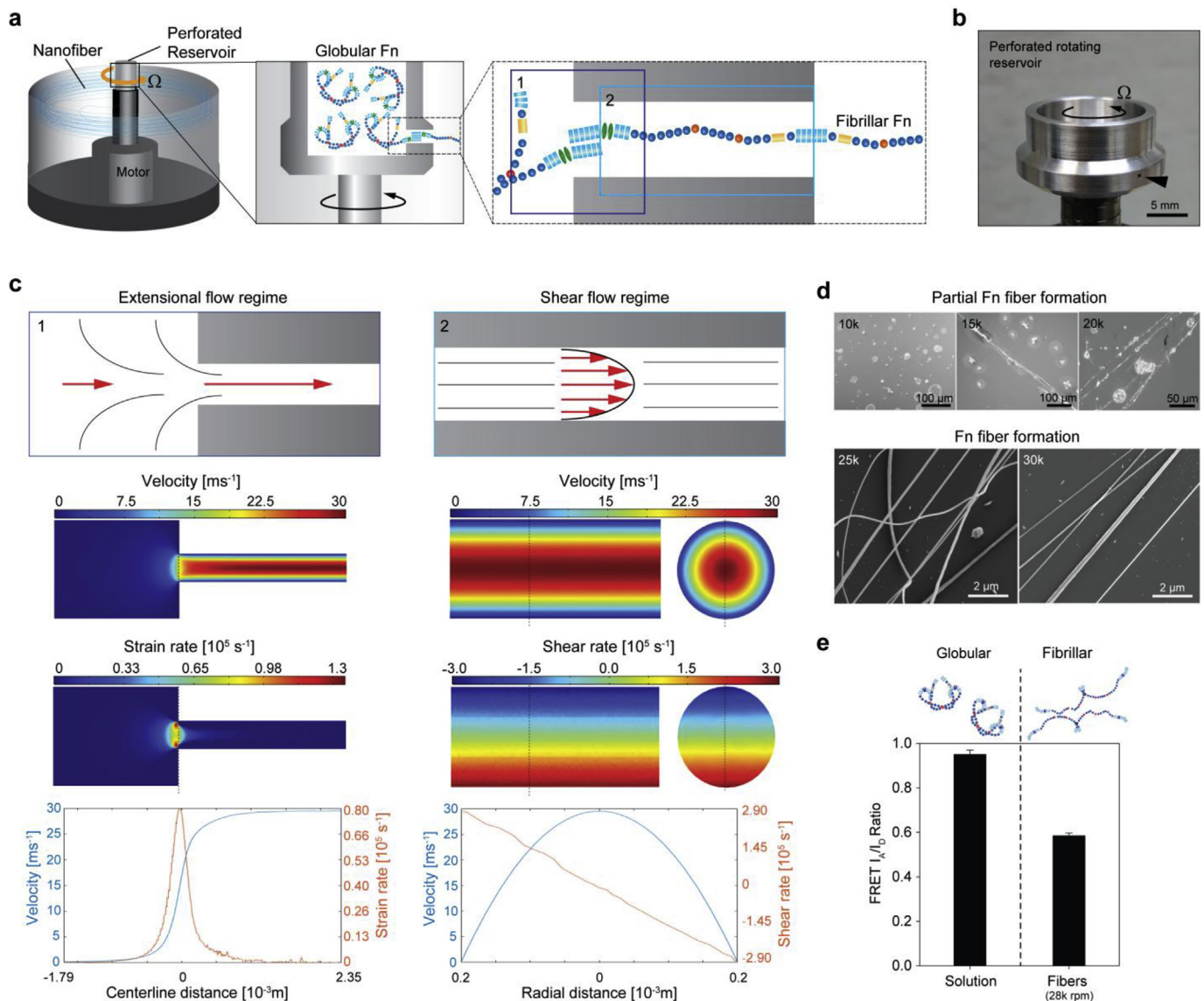
Fig. 1. **Hydrodynamic forces produced via rotary jet spinning drive fibrillogenesis of Fn.** (**a**) The RJS system consists of a perforated reservoir rotating at high speeds. (Insets) Soluble Fn contained in the reservoir is extruded through an orifice and unfolded via centrifugal forces produced by high speed rotation. Insets 1 and 2 show the entry flow and channel flow loci, respectively. (**b**) Image of the perforated reservoir of the RJS system. (**c**) Extensional flow regime schematic (left) at the entry shows the Fn solution experiencing high acceleration and high strain rates, depicted with the CFD simulations below. In contrast, the shear flow regime schematic (right) shows the Fn solution experiencing a high velocity and shear gradient across the channel, demonstrated with the CFD simulations below. (**d**) Scanning electron micrographs (SEM) of Fn spun at different rotation speeds with the RJS. Rotation speeds at 25 k rpm and above show formation of Fn nanofibers, whereas only partial fiber formation is observed at lower speeds. (**e**) Dual-labeling for FRET shows the reduction in acceptor to donor (I_A/I_D) ratio before (Fn solution) and after spinning at 28 k rpm. Intensity ratios were 0.95 ± 0.02 and 0.58 ± 0.01 for the Fn solution and the extended fibrillar Fn, respectively. n > 20 measurements per condition.

Experimentally, we observed that fibers composed of Fn formed at speeds above 25 k rpm with an average fiber diameter of 427 ± 138 nm, while partial fiber formation was noticed for speeds of 15 k to 20 k rpm (Fig. 1d and Fig. S1 and Movie S1). To determine how RJS processing affected the conformation state of Fn, Raman spectroscopy was used and showed an intact secondary structure with defined Amide I and III peaks (Fig. S2). The absence of Amide II peak suggests that Fn tertiary structure was in a partially folded state [42]. To further verify molecular integrity, immunostaining was performed, using an amine-specific fluorophore as well as an antibody against human Fn (Fig. S9). The ability to perform staining of Fn fibers in aqueous solution (see Movies S2) also confirmed their insolubility — distinctive of fibrillar Fn matrices [26]. Together, these data suggest that the RJS system produces sufficient shear

forces to unfold and polymerize Fn, and our spinning parameters are amenable to form fiber scaffolds.

Supplementary video related to this article can be found at https://doi.org/10.1016/j.biomaterials.2018.03.006.

To support these data, we dual-labeled Fn for fluorescence resonance energy transfer (FRET) imaging as previously described [39,40,54], and measured changes in FRET intensity during fiber formation. We observed a high acceptor to donor fluorescence ratio (0.95 ± 0.02) in solution, suggesting Fn in solution is in a compact, folded conformation prior to RJS processing. After spinning, the FRET signal decreased by ~39% to 0.58 ± 0.01 for a rotation speed of 28,000 rpm (Fig. 1e and Fig. S10). As a means of comparison, Fn unfolding using 4 M and 8 M guanidinium chloride [GdnHCl] demonstrated FRET intensities of 0.69 and 0.56, respectively

(Fig. S11). The lower FRET signals ($I_A/I_D < 0.6$) suggests a flow-induced unfolding event, producing insoluble Fn fibers. Collectively, these data indicate that Fn molecules are unfolding — a prerequisite for exposure of Fn-Fn binding sites and induction of fibrillogenesis [26] — and thus validates RJS as a method for producing fibrillar Fn nanofiber scaffolds.

3.2. Fn nanofibers tensile testing

We then asked how these molecular changes impacted the mechanical properties of these fibers. Previously, we showed that extended Fn proteins exhibited bi-modal stress-strain curves when pulled under uniaxial tension [42]. To determine whether the same was true in our Fn networks, we used uniaxial tensile testing to measure the stiffness of these fibers (Fig. 2a and Fig. S3). We attached single fibers to force-calibrated pipette tips and measured deflection at the tip-fiber interface to generate stress-strain curves for our ~400 nm fibers. We observed a 300% strain before failure in our fibers (Fig. 2a and b and Movie S3). To understand how the conformational state of Fn influenced its bulk mechanical properties, we used a two-state eight-chain model to estimate the force-extension profile of a single molecule according to previously reported methods [42]. We observed a plateau and a sharp force increase, suggestive of molecular straightening and domain unfolding, respectively (Fig. 2c). Together with the chemical analysis, the information extrapolated from single fiber mechanics suggests that Fn undergoes conformational unfolding during spinning to yield continuous fibers and that their ability to undergo a 300% strain is largely due to domain unfolding during uniaxial tensile testing.

Supplementary video related to this article can be found at https://doi.org/10.1016/j.biomaterials.2018.03.006.

3.3. In vivo wound closure acceleration

To evaluate the effect of Fn nanofibers on wound healing, we studied full-thickness dorsal wounds in a murine model. Two full-thickness dermal wounds were made with an 8 mm biopsy punch on the flanks of C57BL/6 male mice (Fig. 3a). For optimal integration into cutaneous wounds, native murine dermal ECM was used as the target structural architecture, typically organized in a basket-weave structure on the macroscale and assembled into aligned fiber bundles on the microscale [55] (Fig. 3b, left panel). Here, we collected fibers on a low-speed rotating mandrel post-spinning (~500 rpm) similar to previous methods [35,36,56] to create sub-structures that resemble the basket-woven geometry of native ECM (Fig. 3b, right panel). In this study, fibronectin nanofiber scaffolds (Fn) were compared to a control group with no fibers. Both groups

were covered with Tegaderm™ to secure the wounds and provide support for scaffold integration. Tegaderm™ was chosen as it is a widely used film dressing, known for its moisture retention and protection against pathogens [12], and was therefore added to support both tested conditions. Mice were photographed every two days throughout the study to determine wound closure rate (Fig. 3c). Photographs and wound traces revealed that Fn nanofibers significantly accelerated wound closure within the first 2—4 days post-treatment and remained constant thereafter (Fig. 3 c—e). This accelerated closure rate enabled an earlier wound resolution (closed by ~day 11) compared to the control (~day 14). The macroscopic images further demonstrated that by day 2 post-treatment no excess scaffolds were apparent over the wounds, suggesting that the Fn nanofibers were rapidly integrated and remodelled in the newly forming tissues. Scaffold biodegradation was verified by immunostaining at day 6 (Fig. S12), revealing remnants of Fn fibers in the reforming tissues. This relatively rapid biodegradation may have limited a sustained acceleration throughout the wound closure process. Finally, by day 16, all wounds were fully closed and Fn specimens showed closer morphological appearance to native unwounded tissue (Fig. 3c), suggesting potential for enhanced cutaneous wound healing.

3.4. Dermal and epidermal tissue architecture restoration

Epithelial cells enable de novo regeneration of hair follicles in adult mice after wounding, recapitulating to some extent the embryonic developmental process [44]. We therefore asked whether mimicking the Fn-rich fetal dermal microenvironment in humans promoted restoration of epidermal and dermal architecture, and more specifically if it enhanced neogenesis of skin appendages by stimulating the recruitment of these cells. Tissue sections stained by Masson's trichrome at day 20 revealed that Fn-treated wounds had recovered comparable morphology to healthy native skin (Fig. 4a and b).

Quantitative analysis of skin tissue architecture demonstrated that original, healthy epidermal thickness was recovered for Fn within 20 days, whereas the control wounds still had significantly thicker epidermises, more commonly observed in scarred or diseased tissues [57,58] (Fig. 4c and Fig. S4). Organization of ECM fibers in the dermis, commonly depicted as a basket-woven structure in healthy native tissue and aligned bundles in scar tissue, was used as a metric to assess fibrosis [59,60]. These analyses revealed that both conditions had higher ECM fiber alignment than native skin; however, ECM fiber alignment in the Fn condition was closer to native skin than controls (Fig. 4d). Finally, hair follicle and sebaceous gland density confirmed that Fn-based wound dressings promoted stronger recovery of skin appendage density, and
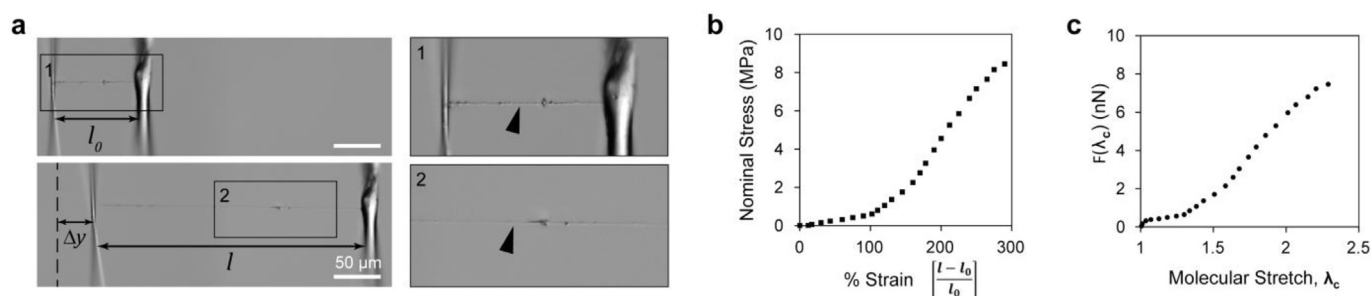
Fig. 2. Fn nanofibers extend 300% and exhibit a bimodal stress strain curve. (a) Differential interference contrast images of a single Fn nanofiber prepared for uniaxial tensile testing (top) and Fn nanofiber during uniaxial tensile testing at ~300% strain (bottom). Inset 1 shows a Fn nanofiber (arrowhead) attached to tensile tester μ-pipettes at the resting position, and inset 2 shows Fn nanofiber under uniaxial tension. (**b**) The stress-strain plot shows that Fn nanofibers produced by RJS have a non-linear behavior, can be characterized by two regimes and can extend up to three times their original length. (**c**) Results of molecular extension estimation by an eight-chain model.
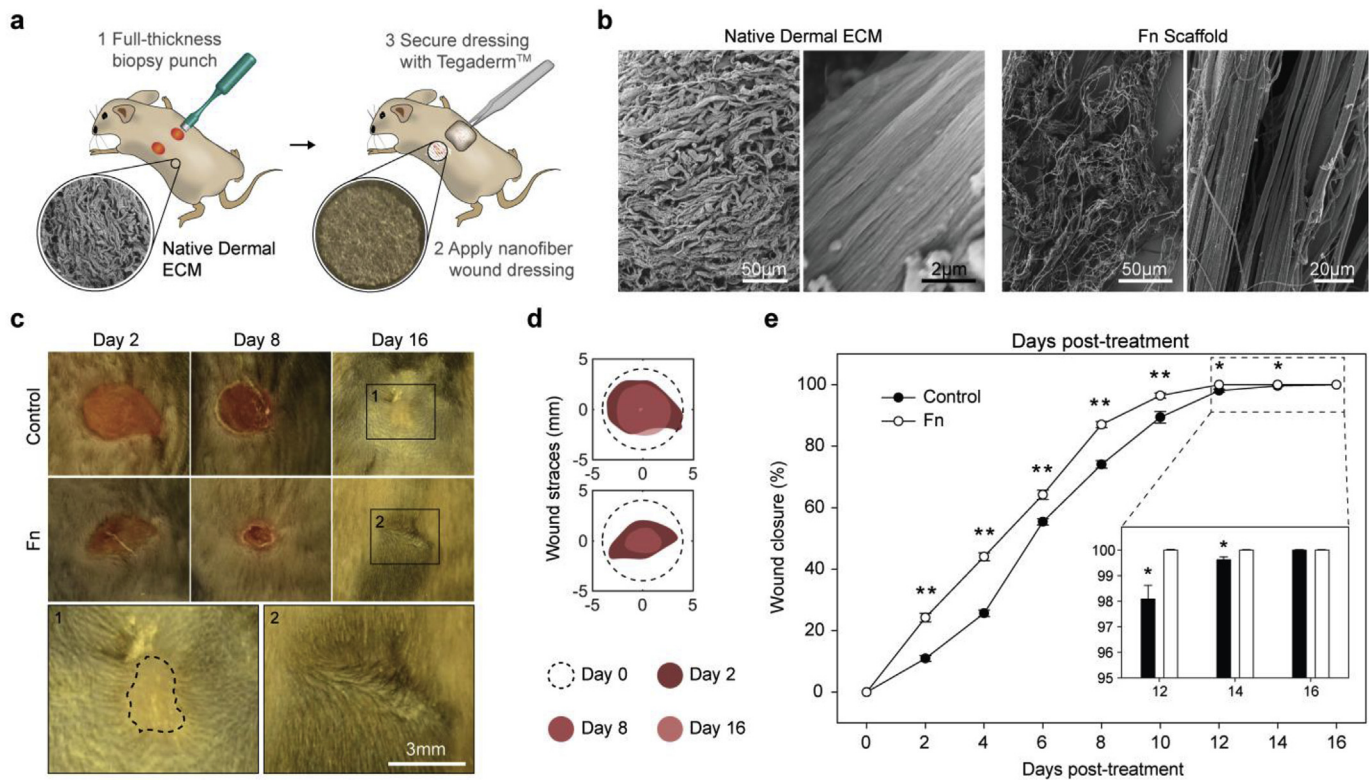
Fig. 3. Fn nanofiber scaffolds accelerated full-thickness wound closure in a C57BL/6 mouse model. (a) Schematic representation of (1) two full-thickness skin wounds on the back of a mouse performed using a biopsy punch and (2) application of a nanofiber wound dressing. To assure adhesion and stabilization of the nanofibers throughout the study, Tegaderm™ film dressings were applied over the nanofiber scaffolds (3). The control group was likewise covered with a Tegaderm™ film. (b) SEMs of the micro- and macro-structure of native dermal ECM inspired the design and fabrication of Fn scaffolds for optimal integration in the wound. (c) Representative images of the non-treated control group and wounds treated with Fn nanofiber dressings at days 2, 8 and 16. Insets bellow show minimal scarring in Fn treatment compared to control (highlighted with the dashed line). (d) From these images, wound edge traces were established for each condition. (e) Normalized wound area over a 16-day period demonstrated that closure rate was significantly increased for Fn dressings compared to the control from day 2 to day 14. Mean and standard error are shown. n = 8 mice and 16 wounds; *p < 0.05 and **p < 0.01 vs. control in a Student's t-test.

showed similar organization to the native state. In contrast, the control group exhibited significantly lower restoration (Fig. 4e and Fig. S4).

To facilitate the assessment of our Fn scaffolds' ability to support tissue architecture recovery, treatments were compared to healthy native skin tissues and scored from 0 to 100% match based on the data from the different testing parameters (Fig. 4f). This analysis highlighted the progress still required in recovering healthy scar-free tissue (in particular, native ECM fiber alignment and hair follicle density), but demonstrated the ability of fibrillar Fn to promote tissue repair with the closest match to native skin for all tested parameters.

Although these results are promising, it should be acknowledged that rodents heal extensively by contraction [61], thus influencing wound closure and repair processes. As such, we performed additional histological H&E staining on Fn-treated skin sections at an earlier time point (day 14 post-wounding) to better assess the respective contributions of tissue contraction and regeneration. While these images clearly evidenced the role of contraction, reducing the effective wound size to approximately 2 mm (Fig. 4g, inset 1), they also revealed Fn-potentiated regeneration. Indeed, re-growing hair follicles originating from the newly formed epidermis were observed at the center of the wound surrounded by epidermal gaps (Fig. 4g, inset 2), corroborating previous neogenesis observations [44]. These preliminary results suggest concurrent activation of contraction and regeneration in this healing process. Continued tissue remodeling may have further

reduced the gaps to minimal levels leading to the native-like skin morphology outcome that we observed by day 20 (Fig. 4b).

3.5. Dermal papillae and basal epithelial cell recruitment

Next, we examined whether dermal papillae (DP), critical for hair follicle neogenesis [62,63], and epidermal cells (EC), which fuel epidermal homeostasis [64] and repair [44], were present in Fn-treated wounds. We stained sectioned tissue samples with alkaline phosphatase (ALP) to determine presence of DP in the bulb of hair follicles, as well as keratin 5 (K5)/keratin 14 (K14) to highlight ECs that constitute the interfollicular epidermis (IFE) and surround hair follicles. Keratin 17 (K17) was additionally used to mark ECs specific to the outer root sheath (ORS) of hair follicles (Fig. 5a and b). After wounding, ECs are recruited from the surrounding IFE and the hair follicle bulge and migrate towards the injury to repair the epidermis and its skin appendages [44]. By day 20, Fn-treated tissues demonstrated widespread presence of K5/K14 in the epidermis and around the hair follicles, while K17 remained specific to the ORS. Remarkably, DPs were discernable in the dermis at the wound edge and at the center of wounds (Fig. 5c). Since skin appendages were largely absent from the centers of control wounds, K5-positive cells were only observed in the IFE while DPs were altogether absent (Fig. S13). Although wound contraction may be hindering our ability to image full structures of hair follicles, the presence of DPs and ECs in Fn-treated tissues is compelling and suggests promise for restoration of functional hair follicles.
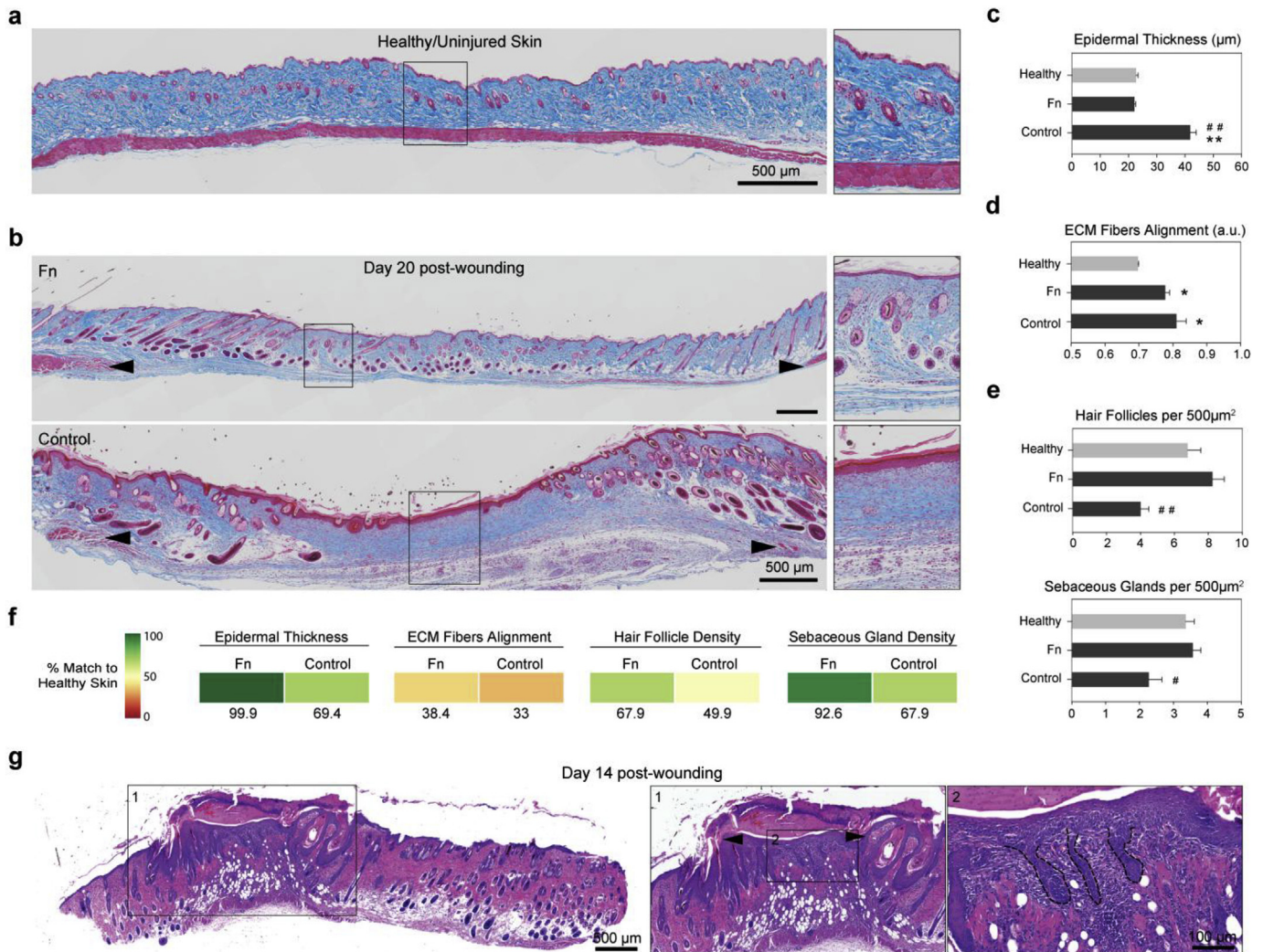
Fig. 4. Fn nanofiber scaffolds promoted native dermal and epidermal architecture recovery. (**a**) Masson's trichrome staining of healthy native tissue sections was performed to establish the design criterion for successful skin tissue restoration. We measured an epidermal thickness of ~20 μm, ECM fiber alignment of ~0.36 (a.u.) as well as ~7 hair follicles and ~3.5 sebaceous glands per surface area of 500 μm^2 (**c–e**). (**b**) Representative stains of skin tissues with different treatment conditions 20 days post wounding. Black arrowheads indicate original wound edges. Insets demonstrate recovery of epidermal thickness and presence of skin appendages at the center of the wound in the Fn-treated tissue, in contrast with the control group. (**c**) Epidermal thickness measurements showed that Fn nanofiber dressings restored tissue close to its healthy state, whereas the control had a statistically significant increase in thickness. (**d**) ECM fiber alignment was used to quantify native tissue (characterized by a basket-woven structure) and scarred tissue (aligned fiber bundles) where 0 is perfectly isotropic and 1 is perfectly anisotropic. Analysis revealed that all recovering tissues were more aligned than native skin, with the Fn condition closer to native skin values than the control. (**e**) Quantification of hair follicles and sebaceous glands per area demonstrated that Fn wound dressings promoted recovery of skin appendage density close to the native state. This restoration was significantly higher than the control group for both hair follicles and sebaceous glands. Mean and standard error are shown. n = 5–8 wounds; **p < 0.01 vs. Healthy and #p < 0.05, ##p < 0.01 vs. Fn in a one-way ANOVA on ranks with a post hoc multiple comparisons Dunn's test. (**f**) To quantify the potency of our treatments, the different parameters measured in **c-e** were compared to native unwounded tissues and score from 0 to 100% match. Colored boxes are used to represent % match to healthy skin. (**g**) H&E sections at day 14 post-wounding reveals that wound contraction and hair follicle regeneration are acting synchronously. Wound contraction is observed by a significantly reduced wound size (from 8 mm to ~2 mm, black arrowheads in inset), while hair follicle neogenesis is confirmed by the presence of hair follicle pegs growing from the new epidermis at the center of the wound.
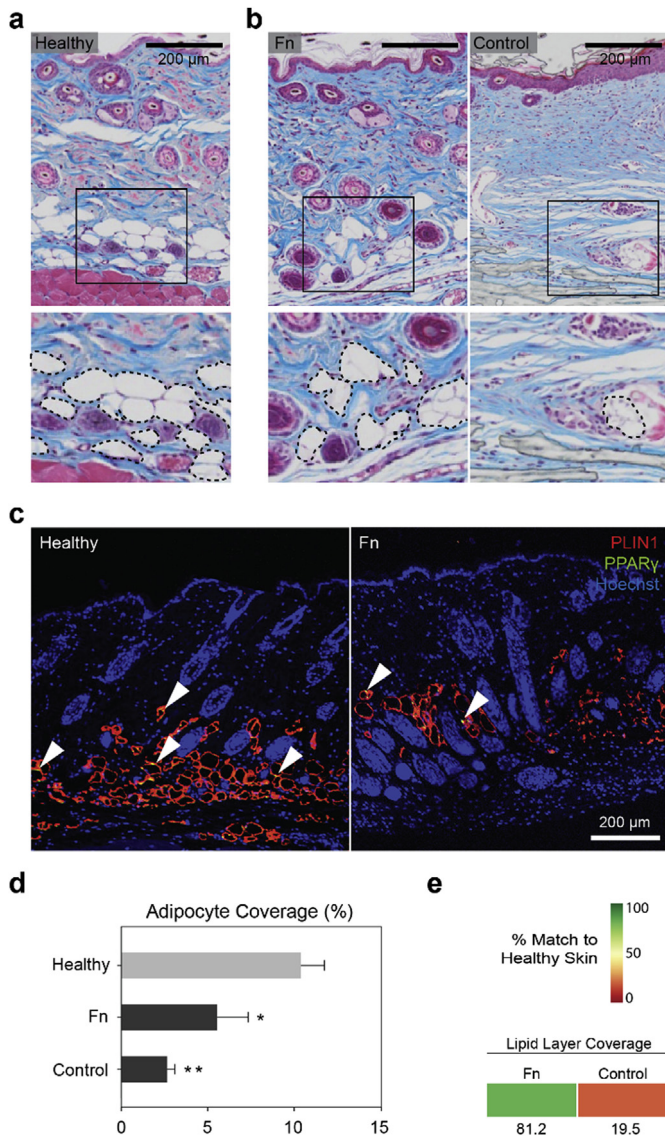
3.6. Lipid layer restoration

We then investigated whether intradermal adipocyte cells, known to contribute to the stem cell niche that directs hair follicle cycling [65], were also recovering to healthy levels in our treated tissues. To verify this, we examined the presence of adipocytes in our Masson's trichrome tissue sections and confirmed this analysis by immunostaining with perilipin-1 (PLIN1), a protein found at the surface of lipid droplets, and peroxisome proliferator activated receptor gamma (PPARγ), a transcription factor expressed in adipocytes. In healthy tissues, lipids are typically observed in the sebum-secreting sebaceous glands, while adipocytes form the lipid layer of the hypodermis (Fig. 6a). After wounding, adipocytes will typically

regrow in the tissue following *de novo* hair follicle neogenesis — approximately 4–5 days after the placodes are first noticed [66]. In Fn-treated wounds, we observed presence of adipocytes reforming the lipid layer in the hypodermis (Fig. 6b and c), thus in agreement with the restoration of mature hair follicle structures at day 20 (see Fig. 5). Distribution and maturation remained however heterogeneous (Fig. 6c), likely caused by measurements from both regenerating adipocytes and adipose tissue drawn via wound contraction (see Fig. 4). A quantitative analysis from the Masson's trichrome sections measured lower levels of adipocytes when compared to healthy skin, indicating that adipose layer restoration was not complete within the 20 day study (Fig. 6d). Conversely, the instructive role of hair follicles on adipocyte regeneration [66] may
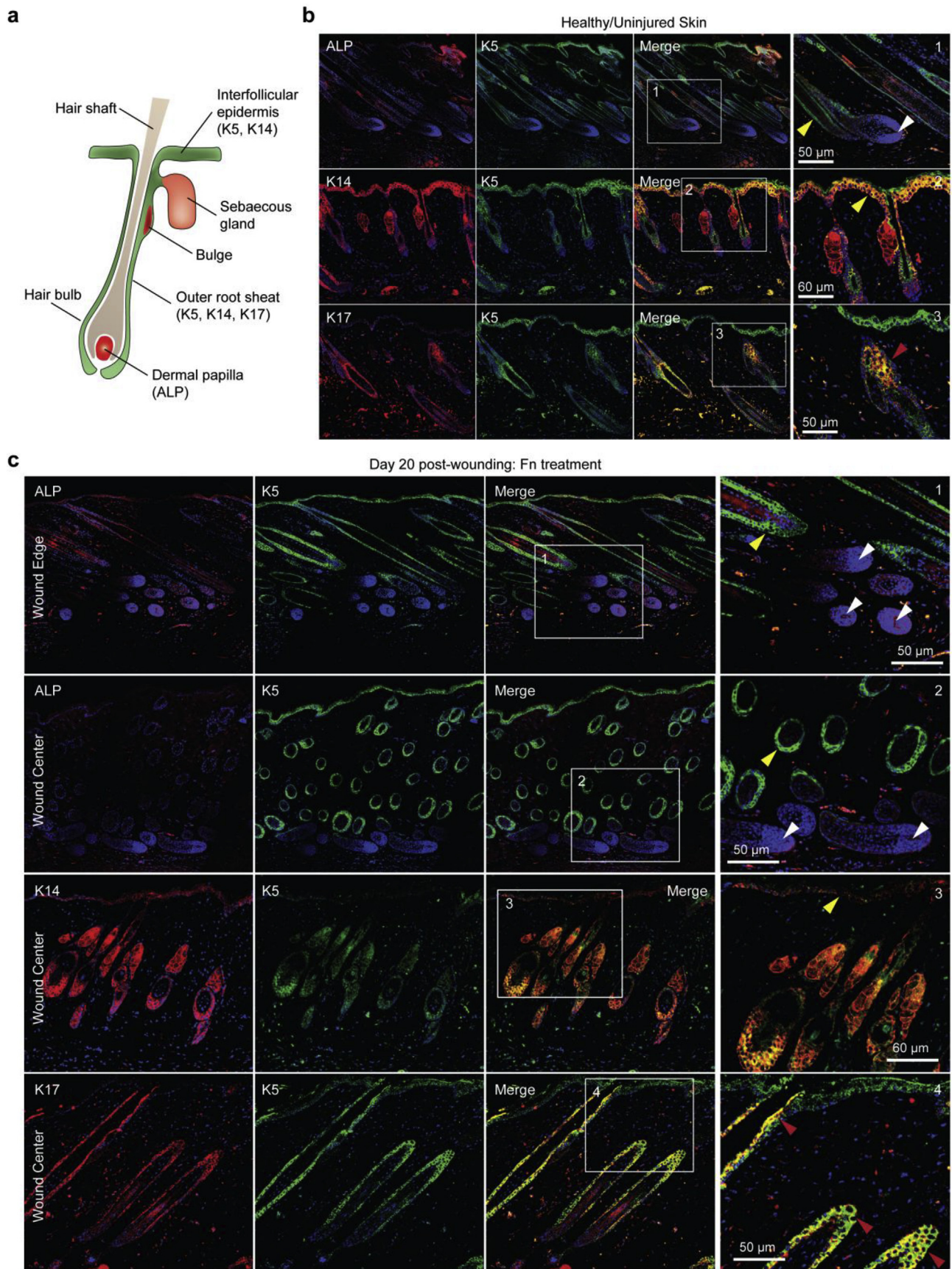
Fig. 5. Fn nanofibers restore dermal papillae and recruit basal epithelial cells. (**a**) Schematic representation of hair follicle structure with specific markers used in (**b**–**c**) labeled. (**b**) Confocal fluorescent images of alkaline phosphatase (ALP) as well as immunostaining with Keratin 5 (K5), Keratin 14 (K14), Keratin 17 (K17) and DAPI confirmed the presence of dermal papillae (DP) and epithelial cells (EC) in healthy tissues of our mouse model. ECs were observed lining the interfollicular epidermis (IFE) and around the hair follicle shaft (yellow arrowheads). ECs with the K17 marker, specific to the outer root sheath (ORS), were observed in hair follicles only (red arrowheads). White arrowheads highlight the presence of DP (stained with ALP) in the follicle bulb, critical for hair growth and cycling. (**c**) At day 20 post wounding, K5/K14-positive cells were observed in the IFE and around hair follicles in tissue sections treated with Fn scaffolds. K17-positive cells were observed exclusively in the ORS. ALP-positive cells were observed in re-formed DP, suggestion potential for restoration of functional hair. For the two first panels (ALP/K5 staining), images close to the wound edge (top) and at the center of the wound (bottom) are shown.

3.7. Skin tissue architecture quality index

As wound healing therapeutics do not only promote wound closure but also attempt to improve tissue repair [2], metrics to evaluate the efficacy of these products is becoming critical. Comparative effectiveness analyses are being developed to improve the understanding of different available wound dressings, helping clinicians choose the ideal treatment [67]. Yet, standardized metrics to assess these treatments at a preclinical stage are still lacking. We therefore developed a *skin tissue architecture quality* (STAQ) index, inspired by previously described statistical methods [48,68], to assess functional and structural recovery of the treated skin tissues. The parameters collected during this study (epidermal thickness, ECM fibers alignment, hair follicle density, sebaceous gland density, adipocyte coverage) were compared to a design criterion — healthy/uninjured skin tissue — and scored from 0 to 100%, where 0 designates the baseline outcome with no distribution overlap and 100 designates the optimal outcome with perfect overlap. STAQ calculations stressed the potential of Fn nanofibers to restore skin structure and functionality with an 84.0% match to healthy skin. In contrast, the non-treated control displayed a smaller overlap of 55.6% (Fig. 7).

Moving forward, additional hallmarks of optimal wound repair and regeneration, as well as clinically relevant parameters should be tested and scored in subsequent studies for a comprehensive potency evaluation. Such metrics could simplify regulatory approval of wound healing and regenerative medicine products, leading to more efficient translations to the market.

4. General discussion and conclusion

Development of Fn nanofiber scaffolds was inspired by the distinct biochemical and biophysical properties of the fetal wound healing microenvironment, and tailored to replicate the multi-scale architecture of native dermis, with a basket-woven scaffold organization, an anisotropic fiber alignment and fibers in the nanometer range. Fabrication of Fn nanofibers was achieved by applying sufficient extensional and shear strain rates to the protein, thus inducing fibrillogenesis at a production-scale level [56]. Additional investigation would however be required to determine the respective influence of each flow regime [49]. FRET analysis was further used to confirm the conformational change instated by RJS.

Fig. 6. Fn promoted restoration of a lipid layer in the wound. (**a**) Masson's trichrome tissue sections were used to identify presence of the adipose layer in healthy native mouse skin. The inset and dashed lines point out the lipid droplet-carrying adipocytes in the hypodermis of the tissue sections. (**b**) Representative staining images showing presence of adipocytes in regenerating tissues treated with Fn and the control. (**c**) PLIN1 and PPARγ immunostaining images of healthy and Fn-treated tissues depicted presence of adipocytes. Arrowheads indicate examples of PPARγ-positive nuclei. (**d**) Quantitative analysis of Masson's trichrome images revealed however that both conditions had significantly lower adipocyte area coverage compared to the healthy skin, with a stronger difference calculated in the control condition. n = 5–8 wounds; *p < 0.05, **p < 0.01 vs. Healthy in a one-way ANOVA on ranks with a post hoc multiple comparisons Holm-Sidak test. (**e**) As previously, treatment conditions were compared to healthy native skin tissue (**d**) and scored from 0 to 100% match. Colored boxes represent % match to native healthy skin.

explain the minimal adipose tissue coverage observed in the control treatment (Fig. 6b), as a low presence of hair follicles was previously measured in this condition (Fig. 4e). As performed previously, treated specimens were scored against a native target to assess their restoration potency. The score highlighted the improvement of Fn-treated tissues over the control, where a 81.2% match was calculated, as opposed to 19.5% for the control. The high Fn score reflects extensive overlap across the distribution of data with healthy skin (see Methods for details).

Fig. 7. Skin tissue architecture quality (STAQ) index. The proposed STAQ index quantifies tissue restoration potentiated by the different tested treatments by scoring critical components of skin tissue architecture from 0 to 100% match to healthy/unwounded skin. The Fn score is compared to the no-treatment control. The combined STAQ values indicate an advantage for the Fn dressings with a score above 80% match to native skin. STAQ analysis highlights the improvements still necessary, in particular the ECM Fibers Alignment and Hair Follicles Density parameters with scores below 80% and 70%, respectively.

When pulled under uniaxial tension, individual fibers showed a bimodal stress-strain curve that the two-state 8-chain model indicated was due to domain unfolding of extended Fn molecules.

These Fn nanofibers, arranged into 8 mm wound dressings, integrated rapidly in the host tissue, while significantly accelerating wound closure and supporting skin tissue restoration. Quantitative histological analysis suggests an improved recovery of dermal and epidermal structures, characterized by closer ECM fiber alignment in the dermis and increased presence of skin appendages throughout the restored tissue. While the role of wound contraction was made evident in this improved outcome, indications of de novo hair follicle regeneration were likewise confirmed at the center of the wounds. In agreement with this, tissues treated with Fn wound dressings exhibited increased abundance of epithelial cells and adipocytes, critical in supporting epidermal and dermal tissue neogenesis and subsequent homeostasis. The STAQ scored the Fn-potentiated tissue restoration at 84.0%. In contrast, the control group (treated with Tegaderm™ only) showed a delayed epidermal thinning, and decreased dermal restoration, characterized by the lower presence of hair follicles and sebaceous glands, and a more anisotropic dermal ECM structure. STAQ score for the non-treated control was measured at 55.6%. Moving forward, integrating clinically-relevant parameters (for example, cost or ease-of-use) as well as clarifying the contributions of wound contraction, re-epithelialization and tissue regeneration will be paramount in establishing a holistic assessment with translational relevance.

Macroscopic and histological analyses moreover indicated a rapid integration and biodegradation of Fn nanofiber dressings within the treated wounds. Although these scaffolds may have had a prolonged influence on tissue restoration by activating several wound healing processes and signaling cascades [24,26], scaffolding support enabling cellular infiltration was in contrast relatively brief. Controlled degradation and remodeling kinetics — as typically required of skin substitutes [69—71] — could enhance tissue ingrowth and prolong functional stimulation. Burn and chronic wounds are for example prone to heal over extended periods of time, thus requiring scaffolds or skin substitutes to support tissue ingrowth and repair over several weeks or more. Recent advances in cross-linked [72,73], annealed [10] or protease-degradable [9] materials have in particular demonstrated sustained physical support, enabling significant regeneration in complex wound healing pathologies. Designing Fn nanofibers to support prolonged tissue ingrowth and remodeling will thus be critical to improve the therapeutic potential of this approach.

To date, reports detailing the use of Fn in regenerative medicine strategies, whether incorporated in delivery vehicles [73] or to functionalize scaffolds [74] have demonstrated strong potency in stimulating a wound healing response in various animal models. Topical treatments of pure Fn have been shown to accelerate wound healing by recruiting host-tissue cells and stimulating endogenous release of growth factors [24,25,75], yet results describing enhanced wound healing and tissue regeneration were limited. In this study, fibrillar Fn nanofibers were able to accelerate wound closure by several days, and histological assessment further recognized their capacity to promote recovery of native-like skin morphology via parallel contributions of wound contraction and tissue regeneration mechanisms.

Ultimately, this study improved the normal outcome of tissue repair by emulating a single constituent in the fetal wound healing microenvironment — the ubiquitous presence of fibrillar Fn. Providing this instructive milieu that attempts to recapitulate the multi-scale structural properties of skin ECM, while delivering functional and protein-binding domains inherent to the Fn molecule, demonstrated strong efficacy for stimulating wound healing and tissue restoration. Bioprotein nanofiber fabrication techniques as described in this study may thus offer a promising new approach toward building highly potent and functional material-based regenerative medicine treatments.

Author contributions

C.O.C, P.H.C, H.M.G and K.K.P designed the study. H.M.G, L.F.D. and C.O.C. developed the materials. A.T.B. developed the computational models. A.T.B., C.O.C. and J.W.R. established the analytical models. H.M.G, C.O.C., L.F.D., J.A.P. and J.W.R. performed characterization of the wound dressing materials. P.H.C and H.M.G performed in vivo experiments. C.O.C., H.M.G, K.G., E.H.A., Y.S.D., S.A. and B.D.P performed in vivo histology staining. C.O.C., H.M.G, S.D., Y.S.D., S.A. and B.D.P performed confocal and brightfield imaging. C.O.C., H.M.G, E.H.A., Y.S.D., A.K.C, A.M.C. performed in vivo data analysis. S.P.S, C.O.C. and S.P.H. developed quality index. C.O.C., H.M.G, A.T.B. and K.K.P. prepared illustrations and wrote the manuscript. A.K.C., L.F.D, Y.S.D., S.P.H., J.W.R., B.D.P., A.M.C. reviewed and corrected manuscript.

Conflict of Interest

The authors declare no competing financial interests.

Acknowledgments

Appendix A. Supplementary data

Supplementary data related to this article can be found at https://doi.org/10.1016/j.biomaterials.2018.03.006.

References

[1] C.K. Sen, et al., Human skin wounds: a major and snowballing threat to public health and the economy, Wound Repair Regen. 17 (2009) 763—771.

[2] G.C. Gurtner, S. Werner, Y. Barrandon, M.T. Longaker, Wound repair and regeneration, Nature 453 (2008) 314–321.
[3] P. Martin, Wound healing–aiming for perfect skin regeneration, Science 276 (1997) 75–81.
[4] D.T. Corr, C.L. Gallant-Behm, N.G. Shrive, D.A. Hart, Biomechanical behavior of scar tissue and uninjured skin in a porcine model, Wound Repair Regen. 17 (2009) 250–259.
[5] J.J. Tomasek, G. Gabbiani, B. Hinz, C. Chaponnier, R.A. Brown, Myofibroblasts and mechano-regulation of connective tissue remodelling, Nat. Rev. Mol. Cell Biol. 3 (2002) 349–363.
[6] K. Lee, J.A. Hubbell, Tissue, cell and engineering, Curr. Opin. Biotechnol. 24 (2013) 827–829.
[7] M.P. Lutolf, J.A. Hubbell, Synthetic biomaterials as instructive extracellular microenvironments for morphogenesis in tissue engineering, Nat. Biotechnol. 23 (2005) 47–55.
[8] M. Guvendiren, J.A. Burdick, Engineering synthetic hydrogel microenvironments to instruct stem cells, Curr. Opin. Biotechnol. 24 (2013) 841–846.
[9] M.P. Lutolf, et al., Synthetic matrix metalloproteinase-sensitive hydrogels for the conduction of tissue regeneration: engineering cell-invasion characteristics, Proc. Natl. Acad. Sci. U. S. A. 100 (2003) 5413–5418.
[10] D.R. Griffin, W.M. Weaver, P.O. Scumpia, D. Di Carlo, T. Segura, Accelerated wound healing by injectable microporous gel scaffolds assembled from annealed building blocks, Nat. Mater. 14 (2015) 737–744, https://doi.org/10.1038/nmat4294.
[11] E.S. Place, N.D. Evans, M.M. Stevens, Complexity in biomaterials for tissue engineering, Nat. Mater. 8 (2009) 457–470.
[12] P.S. Murphy, G.R. Evans, Advances in wound healing: a review of current wound healing products, Plast. Surg. Int. 190436 (2012) 22.
[13] D.A. Banyard, J.M. Bourgeois, A.D. Widgerow, G.R. Evans, Regenerative biomaterials: a review, Plast. Reconstr. Surg. 135 (2015) 1740–1748.
[14] S.P. Zhong, Y.Z. Zhang, C.T. Lim, Tissue scaffolds for skin wound healing and dermal reconstruction, Wiley Interdiscip. Rev. Nanomed. Nanobiotechnol. 2 (2010) 510–525.
[15] U. Rowlatt, Intrauterine wound healing in a 20 week human fetus, Virchows Arch. A Pathol. Anat. Histol. 381 (1979) 353–361.
[1][6] N.A. Coolen, K. Schouten, E. Middelkoop, M.M.W. Ulrich, Comparison between human fetal and adult skin, Arch. Dermatol. Res. 302 (1) (2010 Jan) 47–55, https://doi.org/10.1007/s00403-009-0989-8. Epub 2009 Aug 23.
[17] M.T. Longaker, et al., Studies in fetal wound healing: III. Early deposition of fibronectin distinguishes fetal from adult wound healing, J. Pediatr. Surg. 24 (1989) 799–805.
[18] B.J. Larson, M.T. Longaker, H.P. Lorenz, Scarless fetal wound healing: a basic science review, Plast. Reconstr. Surg. 126 (2010) 1172–1180.
[19] M.R. Namazi, M.K. Fallahzadeh, R.A. Schwartz, Strategies for prevention of scars: what can we learn from fetal skin? Int. J. Dermatol. 50 (2011) 85–93.
[20] Y. Ji, et al., Electrospun three-dimensional hyaluronic acid nanofibrous scaffolds, Biomaterials 27 (2006) 3782–3792.
[21] K. Ghosh, X.D. Ren, X.Z. Shu, G.D. Prestwich, R.A. Clark, Fibronectin functional domains coupled to hyaluronan stimulate adult human dermal fibroblast responses critical for wound healing, Tissue Eng. 12 (2006) 601–613.
[22] D.C. Roy, N.A. Mooney, C.H. Raeman, D. Dalecki, D.C. Hocking, Fibronectin matrix mimetics promote full-thickness wound repair in diabetic mice, Tissue Eng. 19 (Part A) (2013) 2517–2526, https://doi.org/10.1089/ten.TEA.2013.0024.
[23] M.M. Martino, et al., Engineering the growth factor microenvironment with fibronectin domains to promote wound and bone tissue healing, Sci. Transl. Med. 3 (2011), 3002614.
[24] Z. Qiu, A.H. Kwon, Y. Kamiyama, Effects of plasma fibronectin on the healing of full-thickness skin wounds in streptozotocin-induced diabetic rats, J. Surg. Res. 138 (2007) 64–70.
[25] S. Hamed, et al., Fibronectin potentiates topical erythropoietin-induced wound repair in diabetic mice, J. Invest. Dermatol. 131 (2011) 1365–1374.
[26] W.S. To, K.S. Midwood, Plasma and cellular fibronectin: distinct and independent functions during tissue repair, Fibrogenesis Tissue Repair 4 (2011), 1755–1563.
[27] R.A. Clark, K. Ghosh, M.G. Tonnesen, Tissue engineering for cutaneous wounds, J. Invest. Dermatol. 127 (2007) 1018–1029.
[28] E.C. Williams, P.A. Janmey, R.B. Johnson, D.F. Mosher, Fibronectin. Effect of disulfide bond reduction on its physical and functional properties, J. Biol. Chem. 258 (1983) 5911–5914.
[29] K. Sakai, T. Fujii, T. Hayashi, Cell-free formation of disulfide-bonded multimer from isolated plasma fibronectin in the presence of a low concentration of SH reagent under a physiological condition, J. Biochem. 115 (1994) 415–421.
[30] O.S. Ejim, G.W. Blunn, R.A. Brown, Production of artificial-orientated mats and strands from plasma fibronectin: a morphological study, Biomaterials 14 (1993) 743–748.
[31] M.L. Smith, et al., Force-induced unfolding of fibronectin in the extracellular matrix of living cells, PLoS Biol. 5 (2007).
[32] M. Raoufi, et al., Nanopore diameters tune strain in extruded fibronectin fibers, Nano Lett. 15 (2015) 6357–6364, https://doi.org/10.1021/acs.nanolett.5b01356.
[33] D.H. Reneker, A.L. Yarin, Electrospinning jets and polymer nanofibers, Polymer 49 (2008) 2387–2425, https://doi.org/10.1016/j.polymer.2008.02.002.
[34] Z.-M. Huang, Y.-Z. Zhang, M. Kotaki, S. Ramakrishna, A review on polymer nanofibers by electrospinning and their applications in nanocomposites, Compos. Sci. Technol. 63 (2003) 2223–2253.
[35] M.R. Badrossamay, H.A. McIlwee, J.A. Goss, K.K. Parker, Nanofiber assembly by rotary jet-spinning, Nano Lett. 10 (2010) 2257–2261.
[36] M.R. Badrossamay, et al., Engineering hybrid polymer-protein super-aligned nanofibers via rotary jet spinning, Biomaterials 35 (2014) 3188–3197.
[37] P. Mellado, et al., A simple model for nanofiber formation by rotary jet-spinning, Appl. Phys. Lett. 99 (2011), 203107, https://doi.org/10.1063/1.3662015.
[38] H.M. Golecki, et al., Effect of solvent evaporation on fiber morphology in rotary jet spinning, Langmuir 30 (2014) 13369–13374, https://doi.org/10.1021/la5023104 the ACS journal of surfaces and colloids.
[39] G. Baneyx, L. Baugh, V. Vogel, Coexisting conformations of fibronectin in cell culture imaged using fluorescence resonance energy transfer, Proc. Natl. Acad. Sci. U. S. A. 98 (2001) 14464–14468.
[40] W.C. Little, M.L. Smith, U. Ebneter, V. Vogel, Assay to mechanically tune and optically probe fibrillar fibronectin conformations from fully relaxed to breakage, Matrix Biol. 27 (2008) 451–461.
[41] V. Vogel, Mechanotransduction involving multimodular proteins: converting force into biochemical signals, Annu. Rev. Biophys. Biomol. Struct. 35 (2006) 459–488, https://doi.org/10.1146/annurev.biophys.35.040405.102013.
[42] L.F. Deravi, et al., Differential contributions of conformation extension and domain unfolding to properties of fibronectin nanotextiles, Nano Lett. 12 (2012) 5587–5592.
[43] M. Ito, Stem cells in the hair follicle bulge contribute to wound repair but not to homeostasis of the epidermis, Nat. Med. 11 (2005) 1351–1354.
[44] M. Ito, Wnt-dependent de novo hair follicle regeneration in adult mouse skin after wounding, Nature 447 (2007) 316–320.
[45] T.P. Sullivan, W.H. Eaglstein, S.C. Davis, P. Mertz, The pig as a model for human wound healing, Wound Repair Regen. 9 (2001) 66–76.
[46] R. Rezakhaniha, et al., Experimental investigation of collagen waviness and orientation in the arterial adventitia using confocal laser scanning microscopy, Biomechanics Model. Mechanobiol. 11 (2012) 461–473, https://doi.org/10.1007/s10237-011-0325-z.
[47] S.D. Parlee, S.I. Lentz, H. Mori, O.A. MacDougald, Quantifying size and number of adipocytes in adipose tissue, Meth. Enzymol. 537 (2014) 93–122, https://doi.org/10.1016/b978-0-12-411619-1.00006-9.
[48] M.Y. Emmert, et al., Safety and efficacy of cardiopoietic stem cells in the treatment of post-infarction left-ventricular dysfunction - from cardioprotection to functional repair in a translational pig infarction model, Biomaterials 122 (2017) 48–62, https://doi.org/10.1016/j.biomaterials.2016.11.029.
[49] J. Dobson, et al., Inducing protein aggregation by extensional flow, Proc. Natl. Acad. Sci. U. S. A. 114 (2017) 4673–4678, https://doi.org/10.1073/pnas.1702724114.
[50] T.T. Perkins, D.E. Smith, S. Chu, Single polymer dynamics in an elongational flow, Science 276 (1997) 2016.
[51] R.G. Larson, H. Hu, D.E. Smith, S. Chu, Brownian dynamics simulations of a DNA molecule in an extensional flow field, J. Rheol. 43 (1999) 267–304.
[52] D.E. Smith, H.P. Babcock, S. Chu, Single-polymer dynamics in steady shear flow, Science 283 (1999) 1724–1727.
[53] J.S. Hur, E.S.G. Shaqfeh, R.G. Larson, Brownian dynamics simulations of single DNA molecules in shear flow, J. Rheol. 44 (2000) 713–742, https://doi.org/10.1122/1.551115.
[54] S. Ahn, et al., Self-organizing large-scale extracellular-matrix protein networks, Adv. Mater. 27 (2015) 2838–2845.
[55] P.D. Verhaegen, et al., Differences in collagen architecture between keloid, hypertrophic scar, normotrophic scar, and normal skin: an objective histopathological analysis, Wound Repair Regen. 17 (2009) 649–656, https://doi.org/10.1111/j.1524-475X.2009.00533.x official publication of the Wound Healing Society [and] the European Tissue Repair Society.
[56] A.K. Capulli, et al., JetValve: rapid manufacturing of biohybrid scaffolds for biomimetic heart valve replacement, Biomaterials 133 (2017) 229–241, https://doi.org/10.1016/j.biomaterials.2017.04.033.
[57] S.W. Yang, Z.J. Geng, K. Ma, X.Y. Sun, X.B. Fu, Comparison of the histological morphology between normal skin and scar tissue, J. Huazhong Univ. Sci. Technol. 36 (2016) 265–269, https://doi.org/10.1007/s11596-016-1578-7. Medical sciences = Hua zhong ke ji da xue xue bao. Yi xue Ying De wen ban = Huazhong keji daxue xuebao. Yixue Yingdewen ban.
[58] A.A. Tandara, T.A. Mustoe, The role of the epidermis in the control of scarring: evidence for mechanism of action for silicone gel, J. Plast. Reconstr. Aesthetic Surg. JPRAS 61 (2008) 1219–1225, https://doi.org/10.1016/j.bjps.2008.03.022.
[59] M.W. Ferguson, S. O'Kane, Scar-free healing: from embryonic mechanisms to adult therapeutic intervention, Philos. Trans. R. Soc. Lond. Ser. B Biol. Sci. 359 (2004) 839–850, https://doi.org/10.1098/rstb.2004.1475.
[60] M. Xue, C.J. Jackson, Extracellular matrix reorganization during wound healing and its impact on abnormal scarring, Adv. Wound Care 4 (2015) 119–136, https://doi.org/10.1089/wound.2013.0485.
[61] X. Wang, J. Ge, E.E. Tredget, Y. Wu, The mouse excisional wound splinting model, including applications for stem cell transplantation, Nat. Protoc. 8 (2013) 302–309.
[62] A.J. Reynolds, C. Lawrence, P.B. Cserhalmi-Friedman, A.M. Christiano, C.A. Jahoda, Trans-gender induction of hair follicles, Nature 402 (1999) 33–34.
[63] H. Oshima, A. Rochat, C. Kedzia, K. Kobayashi, Y. Barrandon, Morphogenesis and renewal of hair follicles from adult multipotent stem cells, Cell 104 (2001) 233–245.

[64] C. Blanpain, E. Fuchs, Epidermal homeostasis: a balancing act of stem cells in the skin, Nat. Rev. Mol. Cell Biol. 10 (2009) 207—217.

[65] E. Festa, et al., Adipocyte lineage cells contribute to the skin stem cell niche to drive hair cycling, Cell 146 (2011) 761—771.

[66] M.V. Plikus, et al., Regeneration of fat cells from myofibroblasts during wound healing, Science 355 (2017) 748—752, https://doi.org/10.1126/science.aai8792 (New York, N.Y.).

[67] A. Sood, M.S. Granick, N.L. Tomaselli, Wound dressings and comparative effectiveness data, Adv. Wound Care 3 (8) (2014 Aug 1) 511—529.

[68] S.P. Sheehy, et al., Quality metrics for stem cell-derived cardiac myocytes, Stem Cell Rep. 2 (2014) 282—294.

[69] M. Varkey, J. Ding, E.E. Tredget, Advances in skin substitutes-potential of tissue engineered skin for facilitating anti-fibrotic healing, J. Funct. Biomater. 6 (2015) 547—563, https://doi.org/10.3390/jfb6030547.

[70] A.D. Metcalfe, M.W. Ferguson, Tissue engineering of replacement skin: the crossroads of biomaterials, wound healing, embryonic development, stem cells and regeneration, J. R. Soc. Interface 4 (2007) 413—437, https://doi.org/10.1098/rsif.2006.0179.

[71] S. MacNeil, Progress and opportunities for tissue-engineered skin, Nature 445 (2007) 874—880.

[72] G. Sun, et al., Dextran hydrogel scaffolds enhance angiogenic responses and promote complete skin regeneration during burn wound healing, Proc. Natl. Acad. Sci. U.S.A. 108 (2011) 20976—20981, https://doi.org/10.1073/pnas.1115973108.

[73] M.B. Johnson, et al., Topical fibronectin improves wound healing of irradiated skin, Sci. Rep. 7 (2017) 3876, https://doi.org/10.1038/s41598-017-03614-y.

[74] M.M. Martino, et al., Engineering the growth factor microenvironment with fibronectin domains to promote wound and bone tissue healing, Sci. Transl. Med. 3 (2011) 100—189, https://doi.org/10.1126/scitranslmed.3002614.

[75] A.H. Kwon, Z. Qiu, Y. Hirao, Topical application of plasma fibronectin in full-thickness skin wound healing in rats, Exp. Biol. Med. 232 (2007) 935—941 (Maywood, N.J.).